AGU PUBLICATIONS

Geophysical Research Letters

RESEARCH LETTER
10.1002/2013GL058770

Key Points:
- Mountain waves are discovered in the MODIS NIR column water vapor
- We observe 3-4 to 15 km lee waves with an amplitude of 50-70% of the total CWV
- The result is supported by radiosonde and GEOS-5 atmospheric stability analysis

Correspondence to:
A. Lyapustin,
Alexei.I.Lyapustin@nasa.gov

Citation:
Lyapustin, A., M. J. Alexander, L. Ott, A. Molod, B. Holben, J. Susskind, and Y. Wang (2014), Observation of mountain lee waves with MODIS NIR column water vapor, *Geophys. Res. Lett.*, *41*, 710–716, doi:10.1002/2013GL058770.

Received 19 NOV 2013
Accepted 3 JAN 2014
Accepted article online 8 JAN 2014
Published online 30 JAN 2014

Observation of mountain lee waves with MODIS NIR column water vapor

A. Lyapustin[1], M. J. Alexander[2], L. Ott[1], A. Molod[3], B. Holben[1], J. Susskind[1], and Y. Wang[1,4]

[1]NASA Goddard Space Flight Center, Greenbelt, Maryland, USA, [2]NWRA-CoRA Office, Boulder, Colorado, USA, [3]Earth System Science Interdisciplinary Center, University of Maryland, College Park, Maryland, USA, [4]Joint Center for Earth Science Technology, University of Maryland, Baltimore County, Baltimore, Maryland, USA

Abstract Mountain lee waves have been previously observed in data from the Moderate Resolution Imaging Spectroradiometer (MODIS) "water vapor" 6.7 μm channel which has a typical peak sensitivity at 550 hPa in the free troposphere. This paper reports the first observation of mountain waves generated by the Appalachian Mountains in the MODIS total column water vapor (CWV) product derived from near-infrared (NIR) (0.94 μm) measurements, which indicate perturbations very close to the surface. The CWV waves are usually observed during spring and late fall or some summer days with low to moderate CWV (below ~2 cm). The observed lee waves display wavelengths from 3–4 to 15 km with an amplitude of variation often comparable to ~50–70% of the total CWV. Since the bulk of atmospheric water vapor is confined to the boundary layer, this indicates that the impact of these waves extends deep into the boundary layer, and these may be the lowest level signatures of mountain lee waves presently detected by remote sensing over the land.

1. Introduction

Water vapor is a potent greenhouse gas the bulk of which is confined to the boundary layer. It is a major component of the Earth energy and water cycles and a major parameter in weather forecasting and climate modeling. Water vapor responds to surface temperature changes through radiative effects and climate feedbacks [*Trenberth et al.*, 2005; *Wagner et al.*, 2006; *Solomon et al.*, 2010]. Accurate knowledge of atmospheric water vapor is crucial to correct the time delay and phase distortions for the repeat-pass Interferometric Synthetic Aperture Radar applications [e.g., *Li et al.*, 2006, 2009] especially for small-amplitude geophysical signals with long wavelengths, including interseismic deformation and some anthropogenic processes [e.g., *Zebker and Rosen*, 1997]. Satellite and ground-based measurements show that over land it may exhibit large spatial and temporal variability [e.g., *Kumar et al.*, 2010]. A large part of this variability may be related to the airmass transport or evaporation from open water bodies and evapotranspiration of vegetation and soils. In this paper, we report new observations pointing to a mechanism responsible for periodic oscillations in the column water vapor (CWV) related to mountain lee waves.

Atmospheric gravity waves are generated by lower atmospheric sources, e.g., flow over mountains, sporadic diabatic heating in convective systems, and imbalance in jet streams and fronts [*Kim et al.*, 2003]. Mountain lee waves are caused by an air flow over mountain ridges within a stably stratified atmosphere [*Smith*, 1976; *Durran*, 1986]. Breaking waves and small-scale waves can be a source of turbulence and strong vertical air currents, which can be an aviation hazard [*Uhlenbrock et al.*, 2007; *Sharman et al.*, 2012]. Depending on temperature and available moisture, clouds may form in the lee of mountain ranges in rows quasi-parallel to the terrain and orthogonal to the direction of the flow. Satellite classification of orographic clouds began with the first weather satellite, the Television Infrared Operational Satellite, which was launched in 1960 [e.g., *Conover*, 1964]. Since then, many studies reported mountain wave cloud signatures on Earth [e.g., *Fritz*, 1965; *Ernst*, 1976], and even Mars [e.g., *Kahn and Gierasch*, 1982].

Atmospheric gravity waves have been widely studied using high-resolution remotely sensed temperature observations from space. Aqua satellite observations have been used to image and study orographic gravity waves in the stratosphere [e.g., *Wu and Zhang*, 2004; *Eckermann et al.*, 2007; *Alexander and Barnet*, 2007; *Alexander et al.*, 2009; *Alexander and Teitelbaum*, 2011]. Limb Scanning measurements from space also provide observations of stratospheric mountain waves [e.g., *Eckermann and Preusse*, 1999; *Jiang et al.*, 2002; *Alexander et al.*, 2008]. Mountain-generated gravity waves from the Andes observed by the Atmospheric Infrared Sounder have horizontal scales of ~10^2 km and altitudes of ~20–40 km [*Alexander and Barnet*, 2007; *Jiang et al.*, 2013].

Mountain-generated waves are also regularly observed from radiance in 6.7 μm (water vapor) channel with most radiance typically generated at altitudes above approximately 550 hPa [*Uhlenbrock et al.*, 2007; *Feltz et al.*, 2009] where the waves can present aviation hazards.

The high spatial resolution (~1 km) CWV is a remote sensing product of the Moderate Resolution Imaging Spectroradiometer (MODIS) [*Gao and Kaufman*, 2003] and Medium Resolution Imaging Spectrometer [*Bennartz and Fischer*, 2001; *Lindstrot et al.*, 2012]. In this work, we are using column water vapor retrieved as part of the Multi-Angle Implementation of Atmospheric Correction (MAIAC) algorithm developed for MODIS. MAIAC is a new-generation MODIS algorithm which uses a time series analysis and processing of groups of pixels for simultaneous retrievals of atmospheric aerosol and land surface reflectance properties [*Lyapustin et al.*, 2011, 2012]. It includes cloud detection [*Lyapustin et al.*, 2008] as well as a CWV retrieval (based on near-infrared (NIR) channels at 0.94 μm) required for correction of the water vapor absorption. Despite the fact that CWV is an operational MODIS product (MOD05) [*Gao and Kaufman*, 2003], MAIAC also derives CWV because the retrieval algorithm is fast and simple and such an approach helps avoid unnecessary data transfers and cross-product dependence. The MAIAC CWV retrieval approach is described in section 2, followed by a discussion of the mountain waves observed in CWV field in section 3.

2. MAIAC Water Vapor Retrieval

MAIAC retrieves column water vapor over the land surfaces and the inland or coastal waters with glint. The algorithm uses three MODIS NIR water vapor channels with the following band center and width (nm): 17 (905, 30), 18 (936, 10), and 19 (940, 50). The absorption is highest in band 18 and decreases in bands 19 and 17. The retrievals are based on the following approximate formula for the top of atmosphere reflectance:

$$R_\lambda(\mu_0,\mu,\varphi) \cong R^D_\lambda(\mu_0,\mu,\varphi) + \frac{T^{\mathrm{tot}}_\lambda(\mu_0,\mu)}{1-q_\lambda(\mu_0)c_{0,\lambda}}\rho_\lambda(\mu_0,\mu,\varphi), \tag{1}$$

where (μ_0, μ, φ) are cosines of solar and view zenith angles and relative azimuth, R^D_λ is a path reflectance, $T^{\mathrm{tot}}_\lambda(\mu_0,\mu) = \langle T^{\downarrow}(\mu_0)T^{\uparrow}(\mu_0)\rangle_\lambda$ is a total two-way atmospheric transmittance, $c_{0,\lambda}$ is spherical albedo of atmosphere, and $\rho_\lambda(\mu_0,\mu,\varphi)$ and $q_\lambda(\mu_0)$ are surface reflectance and albedo. The terms R^D_λ and T^{tot}_λ are spectrally integrated with the spectral response function of a given channel and solar irradiance. Due to strong water vapor absorption and usually low aerosol scattering in the NIR, the path reflectance and the multiple scattering of light between the surface and the atmosphere (denominator in the second term) can be omitted. If the surface reflectance changes little in a narrow absorption interval of 0.9–0.94 μm, then a two-channel ratio algorithm can be used to derive CWV:

$$\frac{T^{\mathrm{tot}}_{18}}{T^{\mathrm{tot}}_{19}} = \frac{R_{18}}{R_{19}}, \text{ and } \frac{T^{\mathrm{tot}}_{19}}{T^{\mathrm{tot}}_{17}} = \frac{R_{19}}{R_{17}}. \tag{2}$$

For a given view geometry, the solution is found by searching the look-up table (LUT) of transmittance ratio. The LUT was computed with Interpolation and Profile Correction (IPC) algorithm [*Lyapustin*, 2003] designed for fast and accurate radiative transfer computations in absorption bands with arbitrary spectral resolution. The monochromatic water vapor absorption was computed with resolution of 0.01 cm^{-1} based on HITRAN-2000 [*Rothman et al.*, 2003] using the standard atmospheric profiles. To account for different effective absorption and sensitivity of different band ratios, we follow [*Gao and Kaufman*, 2003] and compute the mean water vapor as follows:

$$W = f_1 W_1 + f_2 W_2, \tag{3}$$

where W_i are water vapor values derived from different channel ratios and f_i are weighting functions related to the sensitivities of the two band pairs. They are computed numerically from the ratios $T^{\mathrm{tot}}_{18}(\mu_0,\mu,W)/T^{\mathrm{tot}}_{19}(\mu_0,\mu,W)$ and $T^{\mathrm{tot}}_{19}(\mu_0,\mu,W)/T^{\mathrm{tot}}_{17}(\mu_0,\mu,W)$ stored in the LUT.

The developed algorithm was validated against Aerosol Robotic Network (AERONET) [*Holben et al.*, 1998] CWV ground measurements for 156 stations globally which showed that in cloud-free conditions the retrievals are generally unbiased and accurate to 5–10%. These numbers agree with accuracy assessments of operational MOD05 product. Similarly, we found lower accuracy (20–30%) over areas with red iron-rich soils (e.g., Canberra, Australia), whose reflectance changes considerably in the 0.9–1 μm spectral region due to absorption of the iron compounds. On the other hand, MAIAC CWV is found to be lower than MOD05 by ~5–20%, providing more

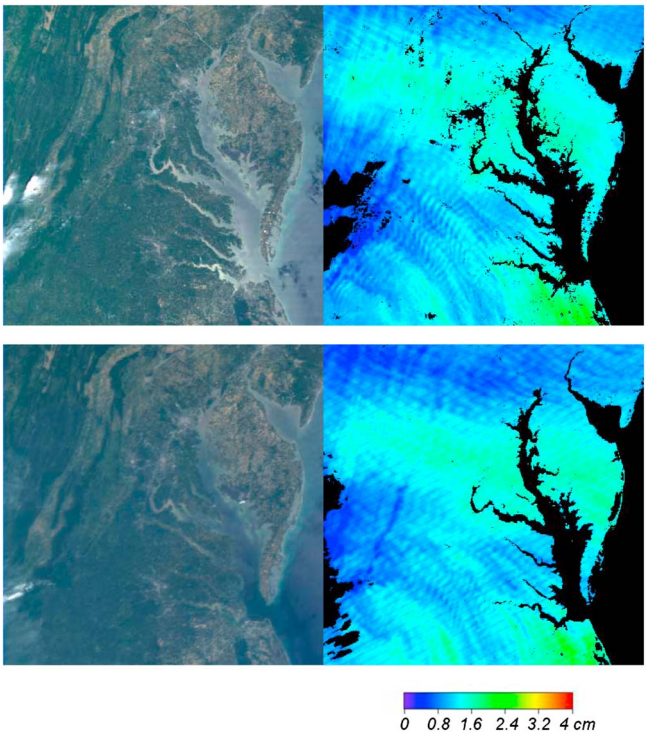

Figure 1. MODIS (top) Terra and (bottom) Aqua RGB and CWV image for the mid-Atlantic U.S. region on 2 June 2011. The difference in Terra-Aqua overpass time is 1 h 40 min.

accurate result. This is confirmed by various MOD05 CWV validation studies against radiosonde, GPS, and Microwave Water Radiometer data showing the wet bias (higher values) of MOD05 product in the same range of ~5–20% [*Liu et al.*, 2013; *Lu et al.*, 2011; *Albert et al.*, 2005; *Li et al.*, 2003; *Prasad and Singh*, 2009; *Kumar et al.*, 2010]. At the same time, validation studies report a very good agreement of AERONET CWV with GPS and radiosonde measurements with $r^2 \sim 0.95$–0.99 [*Liu et al.*, 2013; *Prasad and Singh*, 2009; *Kumar et al.*, 2010]. It is worth mentioning that AERONET CWV algorithm uses WV-band model coefficients generated by the IPC code [*Lyapustin*, 2003] for each individual Sun photometer filter function.

Apart from possible spectroscopy-related differences in computing atmospheric transmittance that removes wet bias, the MAIAC approach is also simpler than MOD05 algorithm. The latter assumes a linear change of surface reflectance across 0.9–0.94 μm interval and uses two additional MODIS channels B2 (0.865 μm) and B5 (1.24 μm) to predict surface reflectance in bands 17–19. *Gao and Kaufman* [2003] assessed the accuracy of the linear model as 2.4–3.9% for most soils, rocks, vegetation, and snow and 8.4% for the iron-rich soils. We tried the *Gao and Kaufman* [2003] five-band approach and found a higher noise, often by a factor of 2–3, than the selected three-band method, based on comparison with AERONET. The error may grow from using much wider spectral interval when the linear spectral model is not a good predictor for the surface reflectance in the 0.85–1.24 μm region.

At high aerosol loading and elevated profiles, the aerosol scattering increases the measured signal and the band ratio thus reducing retrieved CWV [see also *Bennartz and Fischer*, 2001; *Lindstrot et al.*, 2012]. Our AERONET-based analysis shows that high aerosol outbreaks explain over 90% of cases when retrieved WV was significantly lower than the AERONET value. These data show the need for aerosol correction on hazy days which is currently not implemented in either MAIAC or MOD05.

3. Mountain Waves in MODIS CWV

An example of mountain waves in MAIAC NIR CWV is shown in Figure 1. The Terra (top) and Aqua (bottom) images cover an area of $400 \times 400\ km^2$ for 2 June (day of year 153) 2011. The MODIS RGB images (left) show clear conditions with low cloudiness. The average MAIAC aerosol optical depth at 0.47 μm was less than 0.2.

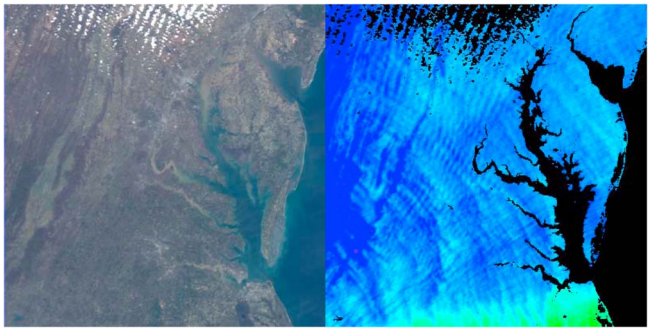

Figure 2. MODIS Aqua RGB and CWV image for 18 March 2011. The color scale is the same as in Figure 1 but with the maximal value of 2.5 cm.

The right images show the retrieved CWV; the black (fill) values correspond to either dark water or detected clouds. The generated wave train roughly parallel to the Appalachian mountains is well visible in the lower-middle part of the image with a dissipation distance of ~150 km. Weaker waves with a larger period can be seen in the northeast section of the Terra CWV image. The Aqua image was obtained 1 h and 40 min after the Terra overpass, so the wave train appears to be stationary. An apparent reduction in contrast in the Aqua CWV relative to the Terra CWV is a consequence of the view geometry, with an Aqua view zenith angle of ~40° as opposed to the nadir view of Terra. In the area of maximal contrast, Terra CWV waves have an average wavelength of ~6 km with an amplitude of ~1.0 cm, with CWV ranging from ~0.5 cm in the trough to ~1.5 cm in the crest.

Figure 2 shows another example from Aqua during 18 March 2011 with wavelength ~7 km, in which cloud formation on the crests of the waves can be seen in the RGB image on the left. Finally, Figure 3 shows two more examples of CWV waves with very different wavelengths, in the range of 3–4 km on 3 June (top) and 10–15 km on 15 October (bottom) of 2011.

Generally, mountain-generated lee waves can be frequently observed east of the Appalachian range during winter, spring, and late fall in the MODIS NIR CWV imagery and on some summer days with low to moderate humidity. On such days, the air of a dry colder upper layer is alternately lifted and lowered by

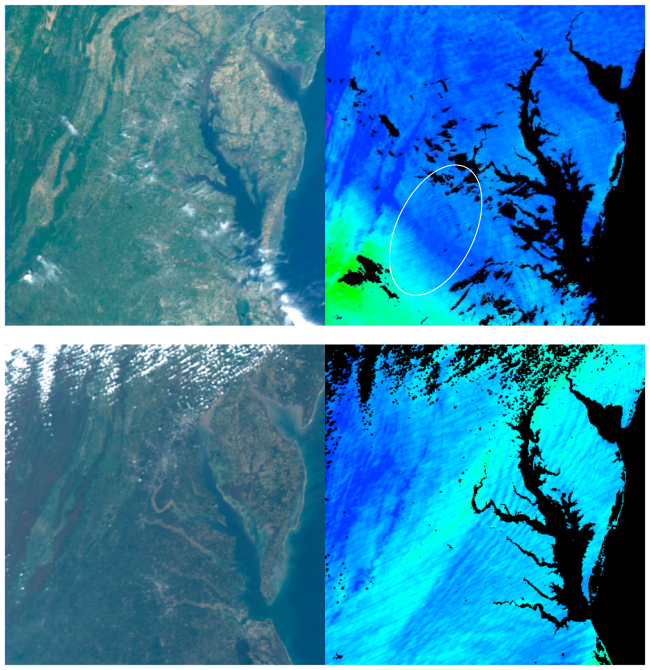

Figure 3. MODIS Aqua RGB and CWV images for (top) 3 June and (bottom) 15 October 2011. The color scale is the same as in Figure 1 but with the maximal values of 2 cm (top) and 2.5 cm (bottom).

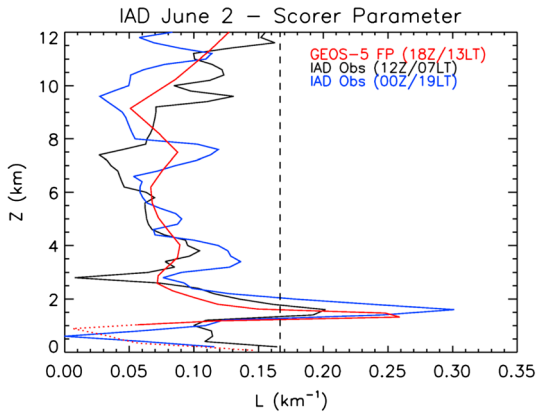

Figure 4. Radiosonde (black and blue) and GEOS-5 (red) derived profiles of the Scorer parameter ($L/2\pi$) at IAD on 2 June. The dotted portion of the GEOS-5 profile indicates the unstable planetary boundary layer (PBL). The dashed line indicates the horizontal wavenumber of the waves observed in MODIS CWV on 2 June.

gravity waves, causing convergence and divergence of air in the warmer moist bottom layer, which is seen as bands in the CWV field.

Atmospheric profiles of temperature and wind fields were used to assess the ability of the atmosphere to sustain trapped gravity waves. The vertical profile of the Scorer parameter (L) calculated as N/U [*Smith*, 1976] from radiosondes and from the GEOS-5 analysis [*Rienecker et al.*, 2008] fields for the 2 June case (Figure 1) is shown in Figure 4. Here N is static stability and U is wind speed approximately normal to wave phase lines. The Scorer parameter [*Scorer*, 1949] arises from the dispersion relation for atmospheric gravity wave solutions to the Taylor-Goldstein equation and is used as an indicator of trapped lee waves. When L decreases strongly with height, trapped lee waves of certain frequencies are possible. The vertical dashed line in the figure is the horizontal wave number ($k = 1$/wavelength) of the wave motions seen in Figure 1, and the level at which L descends below the dashed line gives the trapping height of the gravity waves. Below this level ($L > k$), the waves are trapped or propagate vertically, and above this level ($L < k$) the buoyancy-restoring forces cannot sustain oscillations at those high intrinsic frequencies and the wave motions decay. In addition, the unstable stratification in the atmospheric boundary layer near the surface (the region where the red line is dotted) also cannot sustain gravity waves. The trapped waves, therefore, based on these atmospheric conditions, can exist in a layer between approximately 1 and 2 km above the surface, where enough water vapor exists to reveal oscillations in the CWV of MODIS. Although the waves decay below 1 km according to the analysis, they still penetrate some distance into the moister surface layer. The net result is a series of columns of alternately moister and drier air 1–2 km deep near the surface that are detected by the MODIS sensor. Similar results were found for the other events in Figures 2 and 3, although trapping in a somewhat deeper layer below 3 km was indicated in the October case with the longer horizontal wavelength.

These waves are not observed on typical summer days when CWV values of 3–5 cm are ubiquitous for the East Coast of the U.S. The absence of MODIS CWV observations of mountain lee waves in this season is likely related to deeper unstable PBL heights and atmospheric conditions that will not sustain gravity waves. Higher CWV would also increase the chance of forming clouds that can obscure the waves.

4. Conclusions

Mountain lee waves are an important phenomenon in tropospheric meteorology with practical implications (e.g., aviation hazards). This paper reports the first observation of lee waves in the MODIS NIR column water vapor east of the Appalachian mountains at high 1 km resolution. Generation and vertical propagation of these waves requires a stably stratified atmosphere with stability and wind conditions leading to trapping of shorter horizontal waves. Both radiosonde and atmospheric analysis profiles established that conditions for lee wave trapping below 2–3 km altitude existed on the days when the oscillations in the MODIS CWV were observed. Importantly, in contrast to previous studies based on sounding data which reported gravity waves at altitudes of the midtroposphere and stratosphere, the CWV shows perhaps the lowest near-surface waves that can be detected from remote sensing data over land. Knowledge of variability in CWV at these scales will inform regional and global models of moist processes, which rely on assumptions about the subgrid scale probability distribution functions for total water [e.g., *Molod*, 2012]. Remote sensing measurements of greenhouse gases, such as CO_2 and CH_4, will also benefit from improved characterization of CWV variability because such information allows for more accurate representation of the line broadening by water vapor and potential error reduction in such observations.

Acknowledgments
The research of A. Lyapustin, Y. Wang, and M.J. Alexander was funded by the NASA Program Science of Terra and Aqua (M.J.A. by contract NNH11CD34C).

The Editor thanks Juergen Fischer and an anonymous reviewer for their assistance in evaluating this paper.

References

Albert, P., R. Bennartz, R. Preusker, R. Leinweber, and J. Fischer (2005), Remote sensing of atmospheric water vapor using the Moderate Resolution Imaging Spectroradiometer, *J. Atmos. Oceanic Technol.*, *22*, 309–314, doi:10.1175/JTECH1708.1.

Alexander, M. J., and C. Barnet (2007), Using satellite observations to constrain parameterizations of gravity waves effects for global models, *J. Atmos. Sci.*, *64*, 1652–1665.

Alexander, M. J., H. Teitelbaum, S. Eckermann, J. Gille, J. Barnett, and C. Barnet (2008), High-resolution satellite observations of mountain waves, *Bull. Am. Meteorol. Soc.*, *89*(2), 151–152.

Alexander, M. J., and H. Teitelbaum (2011), Three-dimensional properties of Andes mountain waves observed by satellite: A case study, *J. Geophys. Res.*, *116*, D23110, doi:10.1029/2011JD016151.

Alexander, M. J., S. D. Eckermann, D. Broutman, and J. Ma (2009), Momentum flux estimates for South Georgia Island mountain waves in the stratosphere observed via satellite, *Geophys. Res. Lett.*, *36*, L12816, doi:10.1029/2009GL038587.

Bennartz, R., and J. Fischer (2001), Retrieval of columnar water vapour over land from back-scattered solar radiation using the Medium Resolution Imaging Spectrometer (MERIS), *Remote Sens. Environ.*, *78*, 271–280.

Conover, J. H. (1964), Lee wave clouds photographed from an aircraft and a satellite, *Weather*, *19*, 79–85.

Durran, D. R. (1986), Mountain waves, in *Mesoscale Meteorology and Forecasting*, edited by P. S. Ray, pp. 472–492, Amer. Meteor. Soc., Boston, Mass.

Eckermann, S. D., and P. Preusse (1999), Global measurements of stratospheric mountain waves from space, *Science*, *286*, 1534, doi:10.1126/science.286.5444.1534.

Eckermann, S. D., J. Ma, D. L. Wu, and D. Broutman (2007), A three-dimensional mountain wave imaged in satellite radiance throughout the stratosphere: Evidence of the effects of directional wind shear, *Q. J. R. Meteorol. Soc.*, *133*, 1959–1975.

Ernst, J. A. (1976), SMS-1 nighttime infrared imagery of low-level mountain waves, *Mon. Weather Rev.*, *104*, 207–209.

Feltz, W. F., K. M. Bedka, J. A. Otkin, T. Greenwald, and S. A. Ackerman (2009), Understanding satellite-observed mountain-wave signatures using high-resolution numerical model data, *Weather Forecasting*, *24*(1), 76–86.

Fritz, S. (1965), The significance of mountain lee waves as seen from satellite pictures, *J. Appl. Meteorol.*, *4*, 31–37.

Gao, B. C., and Y. J. Kaufman (2003), Water vapor retrievals using Moderate Resolution Imaging Spectroradiometer (MODIS) near-infrared channels, *J. Geophys. Res.*, *108*(D13), 4389, doi:10.1029/2002JD003023.

Holben, B. N., et al. (1998), AERONET—A federated instrument network and data archive for aerosol characterization, *Remote Sens. Environ.*, *66*, 1–16.

Jiang, J. H., D. L. Wu, and S. D. Eckermann (2002), Upper Atmosphere Research Satellite (UARS) MLS observation of mountain waves over the Andes, *J. Geophys. Res.*, *107*(D20), 8273, doi:10.1029/2002JD002091.

Jiang, Q., J. D. Doyle, A. Reinecke, R. B. Smith, and S. D. Eckermann (2013), A modeling study of stratospheric waves over the Southern Andes and Drake Passage, *J. Atmos. Sci.*, *70*(6), 1668–1689.

Kahn, R., and P. Gierasch (1982), Long cloud observations on Mars and implications for boundary layer characteristics over slopes, *J. Geophys. Res.*, *87*(A2), 867–880.

Kim, Y.-J., S. D. Eckermann, and H.-Y. Chun (2003), An overview of the past, present and future of gravity-wave drag parameterization for numerical climate and weather prediction models, *Atmos. Ocean*, *41*(1), 65–98.

Kumar, S., A. K. Singh, A. K. Anup, and R. P. Singh (2010), Variability of GPS derived water vapor and comparison with MODIS data over the Indo-Gangetic plains, *J. Phys. Chem. Earth*, *55*, 11–18, doi:10.1016/j.pce.2010.03.040.

Li, Z., J.-P. Muller, and P. Cross (2003), Comparison of precipitable water vapor derived from radiosonde, GPS, and Moderate-Resolution Imaging Spectroradiometer measurements, *J. Geophys. Res.*, *108*(D20), 4651, doi:10.1029/2003JD003372.

Li, Z., E. J. Fielding, P. Cross, and J.-P. Muller (2006), Interferometric synthetic aperture radar atmospheric correction: MEdium Resolution Imaging Spectrometer and Advanced Synthetic Aperture Radar integration, *Geophys. Res. Lett.*, *33*, L06816, doi:10.1029/2005GL025299.

Li, Z., E. J. Fielding, P. Cross, and R. Preusker (2009), Advanced InSAR atmospheric correction: MERIS/MODIS combination and stacked water vapour models, *Int. J. Rem. Sens.*, *30*, 3343–3363.

Lindstrot, R., R. Preusker, H. Diedrich, L. Doppler, R. Bennartz, and J. Fischer (2012), 1D-Var retrieval of daytime total columnar water vapour from MERIS measurements, *Atmos. Meas. Tech.*, *5*, 631–646, doi:10.5194/amt-5-631-2012.

Liu, Z., M. S. Wong, J. Nichol, and P. W. Chan (2013), A multi-sensor study of water vapour from radiosonde, MODIS and AERONET: A case study of Hong Kong, *Int. J. Climatol.*, *33*, 109–120.

Lu, N., J. Qin, K. Yang, Y. Gao, X. Xu, and T. Koike (2011), On the use of GPS measurements for Moderate Resolution Imaging Spectrometer precipitable water vapor evaluation over southern Tibet, *J. Geophys. Res.*, *116*, D23117, doi:10.1029/2011JD016160.

Lyapustin, A. (2003), Interpolation and Profile Correction (IPC) method for shortwave radiative transfer in spectral intervals of gaseous absorption, *J. Atmos. Sci.*, *60*, 865–871.

Lyapustin, A., Y. Wang, and R. Frey (2008), An automatic cloud mask algorithm based on time series of MODIS measurements, *J. Geophys. Res.*, *113*, D16207, doi:10.1029/2007JD009641.

Lyapustin, A., Y. Wang, I. Laszlo, R. Kahn, S. Korkin, L. Remer, R. Levy, and J. S. Reid (2011), Multi-angle Implementation of Atmospheric Correction (MAIAC): 2. Aerosol algorithm, *J. Geophys. Res.*, *116*, D03211, doi:10.1029/2010JD014986.

Lyapustin, A., Y. Wang, I. Laszlo, T. Hilker, F. Hall, P. Sellers, J. Tucker, and S. Korkin (2012), Multi-angle Implementation of Atmospheric Correction for MODIS (MAIAC) 3: Atmospheric correction, *Remote Sens. Environ.*, *127*, 385–393, doi:10.1016/j.rse.2012.09.002.

Molod, A. (2012), Constraints on the total water PDF in GCMs from AIRS data and a high resolution model, *J. Clim.*, *25*, 8341–8352.

Prasad, A. K., and R. P. Singh (2009), Validation of MODIS Terra, AIRS, NCEP/DOE, AMIP-II reanalysis-2, and AERONET Sun photometer derived integrated precipitable water vapor using ground-based GPS receivers over India, *J. Geophys. Res.*, *114*, D05107, doi:10.1029/2008/JD011230.

Rienecker, M. M., et al. (2008), The GEOS-5 data assimilation system—Documentation of versions 5.0.1, 5.1.0, and 5.2.0. Technical Report Series on Global Modeling and Data Assimilation, 27.

Rothman, L. S., et al. (2003), The HITRAN molecular spectroscopic database: Edition of 2000 including updates through 2001, *J. Quant. Spectrosc. Radiat. Transfer*, *82*, 5–44.

Scorer, R. S. (1949), Theory of waves in the lee of mountains, *Q. J. R. Meteorol. Soc.*, *6*(323), 41–56.

Sharman, R. D., S. B. Trier, T. P. Lane, and J. D. Doyle (2012), Sources and dynamics of turbulence in the upper troposphere and lower stratosphere: A review, *Geophys. Res. Letters*, *39*, L12803, doi:10.1029/2012GL051996.

Smith, R. B. (1976), The generation of lee waves by the Blue Ridge, *J. Atmos. Sci.*, *33*, 507–519.

Solomon, S., et al. (2010), Contributions of stratospheric water vapor to decadal changes in the rate of global warming, *Science, 327*, 1219, doi:10.1126/science.1182488.

Trenberth, K. E., J. Fasullo, and L. Smith (2005), Trends and variability in column integrated water vapour, *Clim. Dyn.*, *24*, 741–758, doi:10.1007/s00382-005-0017-4.

Uhlenbrock, N. L., K. M. Bedka, W. F. Feltz and S. A. Ackerman (2007), Mountain wave signatures in MODIS 6.7-μm imagery and their relation to pilot reports of turbulence, *Weather Forecasting*, *22*, 662–670, doi:10.1175/WAF1007.1.

Wagner, T., S. Beirle, and M. Grzegorski (2006), Global trends (1996–2003) of total column precipitable water observed by Global Ozone Monitoring Experiment (GOME) on ERS-2 and their relation to near-surface temperature, *J. Geophys. Res.*, *111*, D12102, doi:10.1029/2005JD006523.

Wu, D. L., and F. Zhang (2004), A study of mesoscale gravity waves over the North Atlantic with satellite observations and a mesoscale model, *J. Geophys. Res.*, *109*, D22104, doi:10.1029/2004JD005090.

Zebker, H. A., and P. A. Rosen (1997), Atmospheric artifacts in interferometric SAR surface deformation and topographic maps, *J. Geophys. Res.*, *102*(B4), 7547–7563.